



## Realization of two-sublattice exchange physics in the triangular lattice compound $\text{Ba}_3\text{Er}(\text{BO}_3)_3$

Matthew Ennis<sup>1</sup>, Rabindranath Bag<sup>1</sup>, Chunxiao Liu <sup>2</sup>, Sachith E. Dissanayake<sup>1</sup>, Alexander I. Kolesnikov <sup>3</sup>, Leon Balents<sup>4</sup> & Sara Haravifard <sup>1,5</sup>✉

Geometric frustration commonly occurs in materials where magnetic rare-earth ions are arranged on a two-dimensional triangular lattice. These compounds have been gaining significant attention lately, as they hold the promise of revealing unique quantum states of matter. However, little attention has been devoted to cases where spin- $\frac{1}{2}$  rare-earth ions are substituted with ions exhibiting higher spin multiplicities. Here, we successfully synthesize high-quality single crystal samples of  $\text{Ba}_3\text{Er}(\text{BO}_3)_3$ , which is part of the family of triangular lattice compounds. In our experiments, conducted at extremely low temperatures (around 100 millikelvin), we observe two sublattice exchange interactions in  $\text{Ba}_3\text{Er}(\text{BO}_3)_3$ , resulting in the hexagonal lattice spins exhibiting a mixture of ferromagnetic and antiferromagnetic tendencies. Our theoretical analysis suggest that this behavior may be attributed to the distinct positions of magnetic ions within the crystal lattice. However, the presence of quantum effects adds an extra layer of complexity to our findings, calling for further exploration.

<sup>1</sup>Department of Physics, Duke University, Durham 27708 NC, USA. <sup>2</sup>Department of Physics, University of California, Berkeley 94720 CA, USA. <sup>3</sup>Neutron Scattering Division, Oak Ridge National Laboratory, Oak Ridge 37831 TN, USA. <sup>4</sup>Kavli Institute for Theoretical Physics, University of California, Santa Barbara 93106 CA, USA. <sup>5</sup>Department of Mechanical Engineering and Materials Science, Duke University, Durham 27708 NC, USA. ✉email: [sara.haravifard@duke.edu](mailto:sara.haravifard@duke.edu)

In recent years, there has been growing interest in materials exhibiting geometric frustration due to their potential to support a quantum spin liquid (QSL) state<sup>1,2</sup>. A quantum spin liquid is a unique state of matter where the spins remain highly disordered and fluctuate even at very low temperatures. This frustration commonly occurs in materials where magnetic rare-earth ions are arranged on a two-dimensional triangular lattice. Of these, YbMgGaO<sub>4</sub> has received considerable attention as being a potential host of a quantum spin liquid state<sup>3–7</sup>. However, YbMgGaO<sub>4</sub> has random site mixing between the Mg and Ga atoms, which can make interpretation of the measurements difficult, and has been the source of much debate about the true nature of the ground state<sup>8–11</sup>. This has led to further study of other ytterbium-based triangular materials without site disorder, such as the rare-earth chalcogenides AYbX<sub>2</sub> (A = Na, K, Rb, Cs; X = O, S, Se)<sup>12–20</sup> or the orthoborate materials (Na, K)(Sr, Ba)Yb(BO<sub>3</sub>)<sub>2</sub><sup>21–25</sup>. We have recently reported the single crystal study of another triangular lattice borate compound without site mixing: Ba<sub>3</sub>Yb(BO<sub>3</sub>)<sub>3</sub>, and have found it to exhibit a spin- $\frac{1}{2}$  quantum dipole ground state<sup>26</sup>.

Due to the chemical similarity of the rare-earth elements, different rare-earth elements can be substituted for Yb in the lattice, changing the spin of the magnetic ion without significantly altering the crystal structure. Many of the extensively studied Yb-based triangular materials have also been reported with other rare-earths substituted into the lattice. Some examples are ErMgGaO<sub>4</sub><sup>27</sup> and TmMgGaO<sub>4</sub><sup>28</sup>, the rare-earth chalcogenides ARECh<sub>2</sub> (A = Na, K, Rb; RE = rare-earth; Ch = O, S, Se)<sup>17,29–34</sup> and several examples in the orthoborate family (Na, K)(Sr, Ba)RE(BO<sub>3</sub>)<sub>2</sub> (RE = rare-earth)<sup>22,25,35–37</sup>.

A natural next step in the study of these materials is substituting spin- $\frac{1}{2}$  Yb with spin- $\frac{3}{2}$  Er. Since Er<sup>3+</sup> is also a Kramers ion, it is expected to have a doublet ground state like Yb, so these compounds would provide an opportunity to study the effect of higher spin on the ground states. Both powder and single crystal samples of ErMgGaO<sub>4</sub> have been produced<sup>27</sup> which show similar site mixing to YbMgGaO<sub>4</sub>. Muon spin resonance ( $\mu$ SR) measurements show no signs of ordering down to 25 mK in ErMgGaO<sub>4</sub> and rule out the presence of a glassy state<sup>38</sup>. Inelastic neutron scattering studies have been performed on NaErS<sub>2</sub> and (K, Cs)ErSe<sub>2</sub> to extract the crystal electric field (CEF) parameters; these materials show a large  $J_z = \pm\frac{1}{2}$  component to the ground state, which allows for quantum transitions between the doublet states<sup>39,40</sup>. KErSe<sub>2</sub> was also found to order into a stripe antiferromagnetic state at low temperatures<sup>41</sup> and to host low energy spin-wave-like excitations<sup>42</sup>. Motivated by these reported results and our recent work on Ba<sub>3</sub>Yb(BO<sub>3</sub>)<sub>3</sub><sup>26</sup>, we have begun studies of the analogous compound Ba<sub>3</sub>Er(BO<sub>3</sub>)<sub>3</sub>.

In this study, we detail our efforts in synthesizing both powder and single crystal forms of Ba<sub>3</sub>Er(BO<sub>3</sub>)<sub>3</sub>. We conducted comprehensive magnetic and thermal characterization, complemented by inelastic neutron scattering measurements on this material. These measurements allowed us to derive the CEF spectrum and propose a potential magnetic ground state for Ba<sub>3</sub>Er(BO<sub>3</sub>)<sub>3</sub>. Our examination of single crystals at low temperatures uncovered a potential phase transition occurring at approximately 100 millikelvin. Through symmetry analysis and classical simulation, we propose that Ba<sub>3</sub>Er(BO<sub>3</sub>)<sub>3</sub> exhibits two-sublattice exchange interactions: In this scenario, the spins on a honeycomb lattice exhibit ferromagnetic tendencies due to the presence of additional spins at the hexagonal centers, ultimately leading to an ordered antiferromagnetic phase.

## Results and discussion

**Crystal structure and symmetry considerations.** The double borates form two different crystal structures—trigonal with space

group R $\bar{3}$  or hexagonal with space group P6<sub>3</sub>cm—depending on which rare-earth is used<sup>43</sup>. Ba<sub>3</sub>Er(BO<sub>3</sub>)<sub>3</sub> forms the hexagonal structure with space group P6<sub>3</sub>cm (space group no. 185)<sup>44–46</sup>. The crystal structure is illustrated in Fig. 1a, b. The phase purity of Ba<sub>3</sub>Er(BO<sub>3</sub>)<sub>3</sub> was confirmed using powder x-ray diffraction. Rietveld refinement to the P6<sub>3</sub>cm structure is shown in Supplementary Fig. 1. The corresponding point group is C<sub>6v</sub>, with 12 elements, generated by a three-fold rotation C<sub>3</sub>, a two-fold screw 2<sub>1</sub> along z, and a mirror M. The lattice structure and symmetries are shown in Fig. 1c. The unit cell is spanned by the lattice vectors **a**, **b**, and **c** (see Fig. 1) and contains six Er<sup>3+</sup> ions (two layers  $\times$  three Er<sup>3+</sup> ions in each layer). These Er<sup>3+</sup> ions occupy two distinct Wyckoff positions and have different symmetry properties, as detailed in Table 1. As we will show, the two environments are important in the understanding of magnetic properties of Ba<sub>3</sub>Er(BO<sub>3</sub>)<sub>3</sub>.

**Magnetic susceptibility and magnetization.** Magnetic susceptibility measurements were performed on a single crystal sample with field applied both parallel to the *c*-axis and parallel to the *ab*-plane down to 300 mK using a helium-3 insert, as shown in Fig. 2a. As shown in the inset of Fig. 2a, in both orientations we observe no sharp features in the susceptibility down to 300 mK that would indicate magnetic ordering. The inverse susceptibility data have been fit to the Curie–Weiss law:  $\chi^{-1} = \frac{T-\theta}{C}$ , where  $\theta$  is the Curie–Weiss temperature and *C* is the Curie constant. The inverse susceptibility data and Curie–Weiss fits are shown in Fig. 2b. We performed fits in the high-temperature region (100–300 K) and in the low-temperature region (10–30 K). The fit parameters were used to compute the effective magnetic moment ( $\mu_{\text{eff}}$ ) of the Er<sup>3+</sup> ions. The Curie–Weiss fit in the high-temperature region was also used to calculate the Landé *g*-factor.

In Ba<sub>3</sub>Er(BO<sub>3</sub>)<sub>3</sub> we observe strong directional anisotropy in the susceptibility data. We do not observe any discrepancy between the field-cooled and zero field-cooled data in either orientation. In previously reported triangular compounds Ba<sub>3</sub>Yb(BO<sub>3</sub>)<sub>3</sub>, YbMgGaO<sub>4</sub>, and NaYbBa(BO<sub>3</sub>)<sub>2</sub>, large anisotropy is also observed<sup>4,21,26</sup>. In these compounds the intralayer Yb–Yb distance is less the interlayer distance, and the susceptibility and magnetization is larger with field applied along the *c*-axis, indicating Ising-like spins with an easy axis along the *c*-direction. In Ba<sub>3</sub>Er(BO<sub>3</sub>)<sub>3</sub> the trend is reversed: the susceptibility  $\chi_c$  is smaller than  $\chi_{ab}$ , particularly at low temperatures, as shown in Fig. 2a. This is despite Ba<sub>3</sub>Er(BO<sub>3</sub>)<sub>3</sub> having nearly the same crystal structure as Ba<sub>3</sub>Yb(BO<sub>3</sub>)<sub>3</sub>, with the intralayer Er–Er distance being smaller than the interlayer Er–Er distance (see Table 2). A similar anisotropy ( $\chi_{ab} > \chi_c$ ) is reported the analogous Er-based system ErMgGaO<sub>4</sub> at low temperatures<sup>27,38</sup>. The change in the nature of the anisotropy indicates that the Er spins take on XY-like behavior with an easy-plane perpendicular to the *c*-axis, even though there is no significant change in the crystal structure compared to the Yb compounds. This change in the anisotropic behavior does not occur in all layered triangular systems: in the chalcogenides ARSe<sub>2</sub> (A = Na, K, Cs; R = Yb, Er)  $\chi_{ab} > \chi_c$  regardless of the magnetic ion<sup>12,19,20,30,40,42</sup>, while for NaBaR(BO<sub>3</sub>)<sub>2</sub> (R = Yb, Er)  $\chi_c > \chi_{ab}$  for both Yb and Er<sup>21,36</sup>.

As shown in Fig. 2b, the inverse susceptibility curves for both orientations are nearly parallel from 100 K to 300 K, with  $\theta_{ab} = -3.75$  K and  $\theta_c = -15.46$  K. These values are smaller than those observed in ErMgGaO<sub>4</sub><sup>27</sup>, but are similar to the values observed in the Er chalcogenides NaErCh<sub>2</sub> (Ch = O, S, Se)<sup>17,29,30</sup>. The calculated effective moments and Landé *g*-factors in this region are  $\mu_{\text{eff}}(ab) = 9.02 \mu_B$  and  $g_{ab} = 1.13$  for  $H \parallel ab$  and  $\mu_{\text{eff}}(c) = 9.07 \mu_B$  and  $g_c = 1.13$  for  $H \parallel c$ , in good agreement with the  $\mu = 9.58 \mu_B$  and  $g = 1.2$  expected for a free Er<sup>3+</sup> ion<sup>47</sup>.

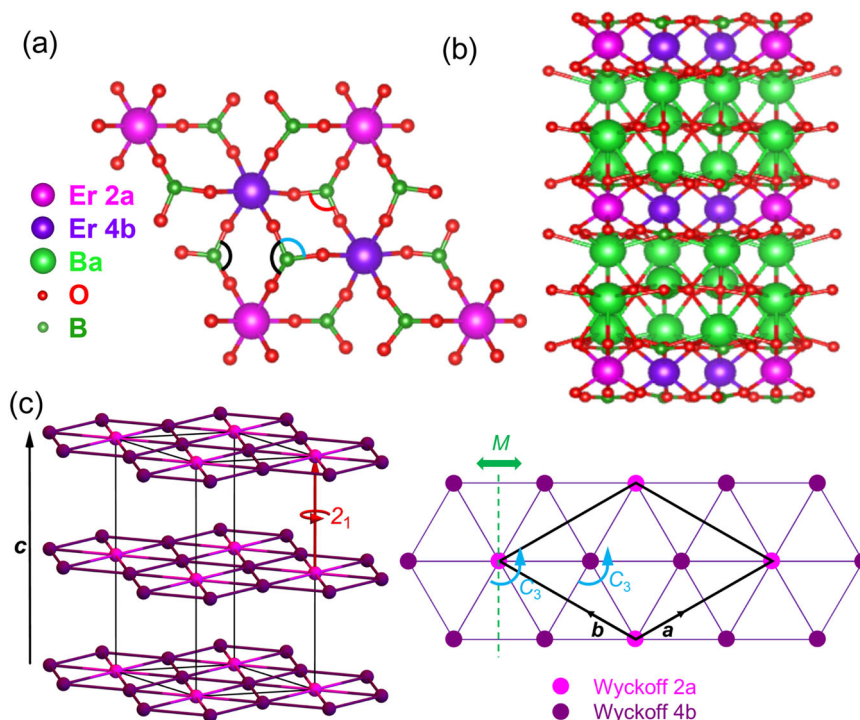


**Fig. 1 Crystal structure, basis vectors and symmetry of  $\text{Ba}_3\text{Er}(\text{BO}_3)_3$ .** **a** Crystal structure of  $\text{Ba}_3\text{Er}(\text{BO}_3)_3$  viewed along the  $c$ -axis, showing the superexchange pathways between the  $\text{Er}^{3+}$  ions. The magenta and purple atoms are the  $2a$  and  $4b$  Er sites, large light green atoms are Ba, small red atoms are O, and small dark green atoms are B. The colored arcs indicate the different O-B-O angles in the two exchanges (black arcs for  $J_{2a}$  and red/blue arcs for  $J_{4b}$ ). **b** Crystal structure viewed along the  $a$ -axis, showing the hexagonal layers of Er atoms, separated by layers of Ba, B, and O atoms). **c** Symmetry operations of the two Er sites. The symmetry operations  $2_1$ ,  $C_3$ , and  $M$  correspond to a 180-degree screw axis in the  $z$ -direction, a three-fold rotation about the  $z$ -axis, and a mirror plane, respectively. The two colors indicate the two Wyckoff positions occupied by the  $\text{Er}^{3+}$  atoms in  $\text{Ba}_3\text{Er}(\text{BO}_3)_3$ .

**Table 1 Wyckoff positions.**

Wyckoff position	Coordinates in basis $a, b, c$	Local symmetry	Symmetry generators
2a	$(0, 0, 0), (0, 0, \frac{1}{2})$	$C_{3v}$	$C_3, M$
4b	$(\frac{1}{3}, \frac{2}{3}, 0), (\frac{2}{3}, \frac{1}{3}, 0),$ $(\frac{1}{3}, \frac{2}{3}, \frac{1}{2}), (\frac{2}{3}, \frac{1}{3}, \frac{1}{2})$	$C_3$	$C_3$

Symmetry information for the two environments of  $\text{Er}^{3+}$  positioned at  $2a$  and  $4b$  sites.

With field applied in the  $ab$ -plane, the inverse susceptibility remains nearly linear down all the way to 300 mK. In contrast, the perpendicular direction is linear down to around 10 K, where it levels off slightly before turning down sharply at 5 K. This downturn behavior is also observed in Yb-based triangular lattice compounds, such as  $\text{Ba}_3\text{Yb}(\text{BO}_3)_3$ ,  $\text{NaYbO}_2$ , and  $\text{NaBaYb}(\text{BO}_3)_3$ <sup>16,17,21,26</sup>, and is believed to be caused by thermal population of CEF levels. The Curie-Weiss fits from 10 K to 30 K give  $\theta_{ab} = -0.1876$  K and  $\mu_{\text{eff}}(ab) = 8.51\mu_B$  for  $H\parallel ab$ , showing a slight decrease in both values for both parameters, and  $\theta_c = -24.16$  K and  $\mu_{\text{eff}}(c) = 9.50\mu_B$  for  $H\parallel c$ . Below 5 K the parameters sharply decrease. The inverse susceptibility remaining nearly linear down to very low temperatures is observed in several other Er-based triangular lattice systems<sup>22,27,29</sup>, and the discrepancy between the low temperature behavior for the two orientations is also seen in single crystals of  $\text{NaErSe}_2$ <sup>30</sup>.

To further investigate the magnetic behavior of this material, isothermal magnetization measurements were carried out at different temperatures ranging from 300 mK to 2 K with field up to 7 T applied parallel to the  $c$ -axis and parallel to the  $ab$ -plane, as shown in Fig. 3a. For both orientations there is a nonlinear region

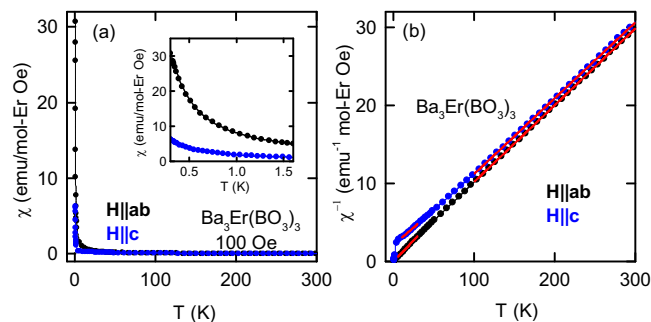


**Fig. 2 Magnetic susceptibility data for  $\text{Ba}_3\text{Er}(\text{BO}_3)_3$ .** **a** Temperature-dependent magnetic susceptibility data for a single crystal sample of  $\text{Ba}_3\text{Er}(\text{BO}_3)_3$ . Black points show data with field applied in-plane ( $\chi_{ab}$ ) and blue points show data with field applied along the  $c$ -axis ( $\chi_c$ ). The inset shows the low-temperature region from 300 mK to 1.6 K, showing the anisotropy in the system. **b** Inverse magnetic susceptibility data are shown. Black points show data with field applied in plane, and blue points show data with field applied along the  $c$ -axis. Red lines show the fit to the Curie-Weiss law.

at low field where the magnetization rapidly increases before the curve becomes nearly linear above 3 T. With field applied in the  $ab$ -plane, the magnetization increases quickly at first and then slowly tapers off as the field increases. In contrast, with field applied along the  $c$ -axis the magnetization begins to level off around 1 T before increasing again. This behavior can be seen more clearly in the plot of  $dM/dH$  shown in Fig. 3b. The  $dM/dH$  curve goes down to a local minimum at 1 T, then rises to a local maximum at 3 T before going back down at higher fields. As with susceptibility, the magnetization data shows strong anisotropy in

**Table 2 Distances and exchange parameters.**

Intra-layer bonds	4b-4b	4b-2a	2a-2a and 4b-4b
Bond distance	5.47315 Å	5.47403 Å	9.00139 Å
Exchange energy	$J_{4b}$	$J_{2a}$	$J_3$
Inter-layer bond	4b-4b and 2a-2a		
Bond distance	9.48007 Å		
Exchange energy	$J_{u-d}$		

Distances between  $\text{Er}^{3+}$  ions and definition of exchange parameters for intra-layer and inter-layer bonds.

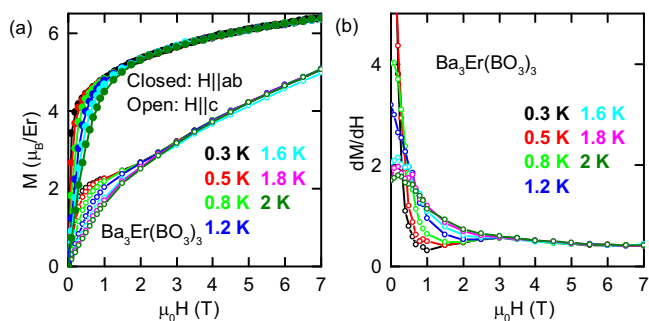


**Fig. 3 Magnetization data for  $\text{Ba}_3\text{Er}(\text{BO}_3)_3$ .** **a** Isothermal magnetization data of  $\text{Ba}_3\text{Er}(\text{BO}_3)_3$  taken at various temperatures. Closed points show data with field applied in-plane and open points show data with field applied along the  $c$ -axis. The different colors indicate the temperatures of the measurements. **b** First derivative of isothermal magnetization with field applied along the  $c$ -axis showing anomaly between 1 T and 3 T, with colors representing the same temperatures as in **a**.

this material. Similar anisotropy in the saturated magnetization and curve shape are observed in  $\text{ErMgGaO}_4$  (where a crossing of the magnetization curves is also observed) and  $\text{AErSe}_2$  ( $A = \text{Na}$  and  $\text{K}$ )<sup>27,30</sup>.

**Heat capacity.** To further characterize this material, we also performed heat capacity measurements at various fields from room temperature down to 60 mK using helium-4 and dilution refrigerator (DR) setups. The measurements were carried out on a single crystal sample of  $\text{Ba}_3\text{Er}(\text{BO}_3)_3$  with field applied parallel to the  $c$ -axis. The heat capacity data up to 15 K with several applied fields (0 T, 0.25 T, 0.5 T, 1 T, 3 T) are shown in Fig. 4a. Our heat capacity setup requires thin, flat samples where field is applied perpendicular to the surface of the sample.  $\text{Ba}_3\text{Er}(\text{BO}_3)_3$  cleaves easily between the  $ab$ -planes, so we were unable to produce a sample with the correct dimensions and orientation to measure the heat capacity with field applied in-plane.

The zero field data shows a sharp peak at 0.1 K, possibly indicating the onset of magnetic order. The peak broadens and shifts to higher temperature with increasing field strength, and appears more like a two-level Schottky anomaly. In order to further study the transition between the sharp peak and broad features, we measured the heat capacity while increasing the applied field in small steps. For clarity, the fields below 1 T are shown separately in Fig. 4b for the low-temperature region up to 1.5 K. As the field is slowly increased up to 0.1 T, the intensity of the peak decreases but the peak's position at 0.1 K does not change. As the field is further increased beyond 0.15 T, the peak begins to broaden and shift to higher temperatures, matching the behavior we observed for the higher fields. We are planning a follow-up neutron powder diffraction measurement to confirm

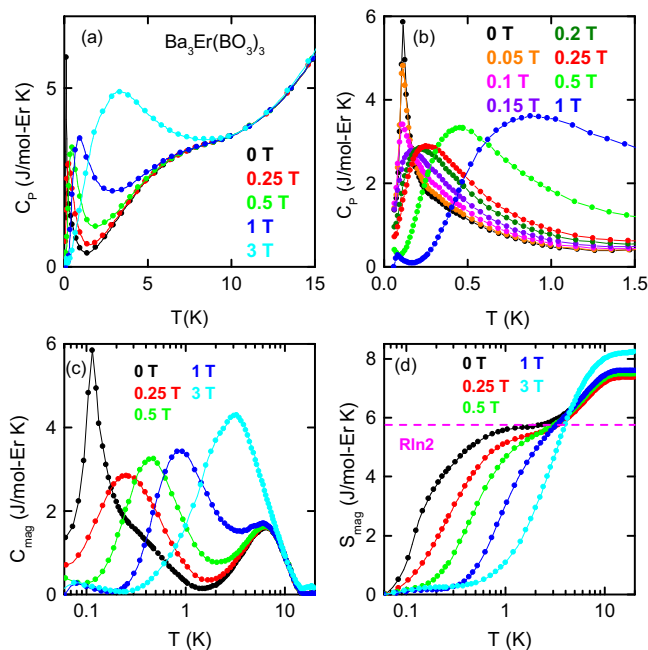


**Fig. 4 Field-dependent thermal measurements of  $\text{Ba}_3\text{Er}(\text{BO}_3)_3$ .** Colors represent different fields applied during measurements. **a** Heat capacity of  $\text{Ba}_3\text{Er}(\text{BO}_3)_3$  at various fields applied along  $c$ -axis, up to 15 K. **b** Low-temperature heat capacity data with field applied in smaller increments. **c** Magnetic heat capacity of  $\text{Ba}_3\text{Er}(\text{BO}_3)_3$  obtained by subtracting  $T^3$  fit to the 0 T data. **d** Magnetic entropy up to 20 K. The dashed line indicates entropy of  $R \ln 2$ . Note that **c** and **d** are plotted on a log scale to better show the low temperature behavior.

the nature of the ordering and determine the magnetic structure at low temperatures. We consider this to be outside the scope of the current paper and plan to present those results in a future publication.

The magnetic heat capacity and corresponding magnetic entropy are shown in Fig. 4c, d. The lattice contribution to the heat capacity was estimated by fitting the zero field data to a cubic model ( $T^3$ ), which was subtracted to obtain the magnetic heat capacity ( $C_{\text{mag}}$ ). The magnetic heat capacity of  $\text{Ba}_3\text{Er}(\text{BO}_3)_3$  reveals a low-temperature peak that shifts to higher temperature with increasing field, which lines up with the Schottky-like feature we observe. We also observe a peak centered at 6.5 K which is present for all fields measured.

The entropy as a function of temperature [see Fig. 4d] shows a plateau at around 2 K, with a value of  $R \ln 2 \sim 5.76 \text{ J mol}^{-1} \text{ K}^{-1}$ . This indicates that there is an effective two-level state at very low energy, agreeing with the prediction of a Kramers' doublet ground state<sup>39,40</sup>. Furthermore, another plateau is observed at about 10 K, with an entropy value about  $\frac{4}{3} R \ln 2 \sim 7.68 \text{ J mol}^{-1} \text{ K}^{-1}$ . If we assume that this peak is due to another CEF doublet, we should expect to see the entropy increase by  $R \ln 2$  above the previous plateau. However, the entropy only increases by  $\frac{1}{3} R \ln 2$  over the ground state doublet, so this doublet must only be associated with one-third of the Er ions. We associate this CEF excitation with the Er atoms at Wyckoff position 2a, which indeed comprise one-third of the total Er atoms.

**Neutron scattering measurements.** To get a better understanding of the CEF spectrum of  $\text{Ba}_3\text{Er}(\text{BO}_3)_3$ , inelastic neutron scattering measurements were carried out on a powder sample at the SEQUOIA time-of-flight spectrometer at Oak Ridge National Laboratory<sup>48</sup>. Measurements were performed with incident

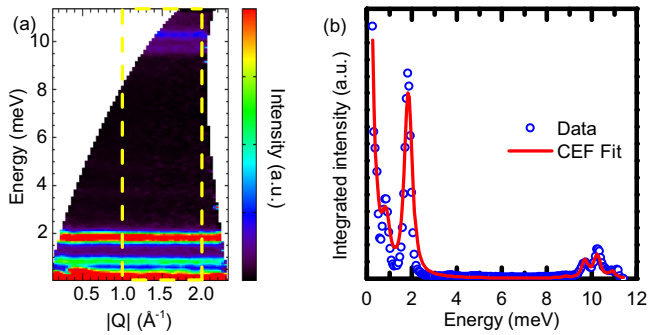


**Fig. 5** Neutron scattering data of  $\text{Ba}_3\text{Er}(\text{BO}_3)_3$ . **a** Inelastic neutron scattering (INS) data taken on a powder sample of  $\text{Ba}_3\text{Er}(\text{BO}_3)_3$  at 5 K. **b** Blue points show integrated intensity from the boxed region in **a**. The red line shows the Stevens operator fit to the data.

energies 150 meV, 50 meV, and 12 meV, at temperatures 5 K, 30 K and 150 K. The neutron spectra for all data sets are given in Supplementary Fig. 2.  $\text{Er}^{3+}$  has  $S = \frac{3}{2}$ —so all of its energy levels are Kramers doublets—and has  $J = \frac{15}{2}$ —so one would expect to see a total of 7 excitations above the ground state. Our data show two low-energy excitations at 0.8 and 1.9 meV and two higher-energy excitations around 10 meV as shown in Fig. 5a. Additionally, we see signatures of two closely lying excitations at higher energies of approximately 12.5 and 13.5 meV—see Supplementary Fig. 2. The neutron spectrum with  $E_i = 12$  meV taken at 5 K and a line cut to show the intensity as a function of energy are shown in Fig. 5. The first excitation at 0.8 meV corresponds to a temperature of 9.3 K which coincides with the broad feature we observe in the magnetic heat capacity measurements [see Fig. 4c]. The next excitation occurs at 1.9 meV which corresponds to a temperature of 22 K, which matches with the small peak in the magnetic heat capacity we see at the highest temperatures of our measurement. The CEF spectrum we observe is similar to the values calculated for  $\text{ErMgGaO}_4$  and  $\text{Ba}_3\text{ErB}_9\text{O}_{18}$ , (although the excitations tend to appear at slightly lower energies in  $\text{Ba}_3\text{Er}(\text{BO}_3)_3$  than in either of these materials)<sup>38,49</sup>, and for those observed in  $\text{NaErS}_2$  and  $\text{KerSe}_2$ <sup>39,40</sup>.

The low energy levels observed in the magnetic heat capacity and inelastic neutron scattering are captured by the CEF Hamiltonian  $H$ . The two Er sites have different point symmetries, so depending on the local symmetry being  $C_3$  (for 4b positions) or  $C_{3v}$  (for 2a positions), we have

$$H_{4b} = B_2^0 O_{2,0} + B_4^0 O_{4,0} + B_4^3 O_{4,3} + B_4^{-3} O_{4,-3} + B_6^0 O_{6,0} + B_6^3 O_{6,3} + B_6^{-3} O_{6,-3} + B_6^6 O_{6,6} + B_6^{-6} O_{6,-6} \quad (1a)$$

$$H_{2a} = B_2^0 O_{2,0} + B_4^0 O_{4,0} + B_4^3 O_{4,3} + B_4^0 O_{6,0} + B_6^3 O_{6,3} + B_6^6 O_{6,6} \quad (1b)$$

Here  $O_{n,m}$  are the standard Stevens operators<sup>50</sup>, and  $B_n^m$  are the Stevens parameters to be determined. We perform a point charge calculation to obtain the Stevens parameters and the CEF levels<sup>51</sup> (for further details on the calculation, see Supplementary Note 3 and Supplementary Fig. 4). See ref.<sup>52</sup> for derivation. For the ion positions we use the data from the Materials Project<sup>53,54</sup>. We consider the following two models:

- The Ba-Er-B-O model: We calculate the CEF contribution from all types of ions.
- The O-only model: We only include the CEF contribution from the oxygen ions  $\text{O}^{2-}$ . This describes the scenario in which the CEF is mainly due to the ligands.

The results are shown in Table 3. The Ba-Er-B-O model gives comparable CEF levels for  $\text{Er}^{3+}$  in both the 2a and 4b environments. On the other hand, the O-only model has the first CEF excitation for the 2a position at  $E_1 = 0.2322$  meV (2.7 K) and for the 4b position at 1.156 meV (13.4 K); as a result, it provides one scenario where the 2a has a significantly lower first CEF excitation, in agreement with the CEF result from the entropy analysis. We point out that the point charge model so far involves no fitting parameters, yet already shows qualitative agreement with the experimental result.

To further quantitatively improve our result, we include a radial factor  $\gamma$  in the O-only model to control the ion's radius. As one can see, the O-only model with a radial factor  $\gamma = 1.1$  reproduces the low energy CEF levels extracted experimentally quite well. For comparison, we also fit CEF Hamiltonian directly to our neutron data, using the point charge calculations as a guide for which peaks to fit to which ion. The result of that fit is also given in Table 3 for comparison and the fit is shown in Fig. 5b. However, we note that this fit is likely unreliable: since we only observe 4 distinct peaks in our data, the fit is largely unconstrained and gives several additional transitions at higher energies which we do not observe in our neutron data (details on the data fitting and comparison of the three models to the neutron data are given in Supplementary Note 2, and the results are shown in Supplementary Fig. 3). While the O-only model seems to give a good estimate of the CEF levels, we point out two potential issues: (1) it is yet to find a reason why keeping only the anions ( $\text{O}^{2-}$ ) improves the modeling. Naively this describes the situation where the positive charges from the cations are maximally screened; such screening effect is beyond a point charge description. (2) We note that the Stevens parameters from the point charge model show a large difference from the experimental values (particularly in the values of the 4a Er site). More experimental data are needed in order to better understand the crystal field physics. To summarize, a point charge model for the CEF levels from only  $\text{O}^{2-}$  contributions qualitatively reproduces the magnetic heat capacity at low temperature due to the ground state Kramers pair and low energy first excitation Kramers pair only for Wyckoff position 2a.

**Exchange physics.** The low energy physics in the temperature range  $0 \text{ K} < T < 11 \text{ K}$  happens in the ground state doublet and the first excited doublet for the 2a position ions. If we restrict to a smaller temperature range  $0 \text{ K} < T < 2 \text{ K}$ , the physics happens purely in the ground state doublet. In this section we focus on the smaller temperature range  $0 \text{ K} < T < 2 \text{ K}$ . Our goal is to analyze the possible spin Hamiltonian consistent with the experimentally observed magnetic heat capacity. At nearest-neighbor level there are two types of exchanges: those connecting two 4b sites, which we call  $J_{4b}$ , and those connecting 2a and 4b, which we call  $J_{2a}$ . See Table 2 for more information. The triangular lattice can be viewed as a honeycomb lattice of 4b ions decorated by a (larger) triangular lattice of 2a ions located at the hexagon centers; see Fig. 1c for an illustration. The exchange pathways for  $J_{2a}$  and  $J_{4b}$  are both Er-O-B-O-Er, although the structure of those pathways are different (see Fig. 1a). In addition to the different symmetries of the two Er sites, the O-B-O bond angles are different along the two exchange pathways: between the 2a and 4b sites both angles are  $125^\circ$ , while the two angles between the two 4b sites are  $105^\circ$  and  $109^\circ$ . Because the 2a and 4b sites have different crystallographic environments, the exchanges  $J_{4b}$  and  $J_{2a}$  can have different energy scales. This phenomenon of different exchange parameters for different Wyckoff sites was calculated for another hexagonal rare-earth compound  $\text{GdInO}_3$ , where it was hypothesized that the different interactions between the sites lead to

**Table 3 Experimental and theoretical comparison.**

Model: Ba-Er-B-O

2a levels (meV):  $E_1 = 4.390, E_2 = 12.43, E_3 = 22.79, E_4 = 34.54, E_5 = 49.44, E_6 = 55.93, E_7 = 57.67$ 4b levels (meV):  $E_1 = 4.458, E_2 = 12.59, E_3 = 22.95, E_4 = 34.63, E_5 = 49.51, E_6 = 55.71, E_7 = 57.41$ 

Position	$B_2^0$	$B_4^0$	$B_4^3$	$B_4^{-3}$	$B_6^0$	$B_6^3$	$B_6^{-3}$	$B_6^6$	$B_6^{-6}$
2a	0.293	-0.000572	0.0146	0	$8.30 \times 10^{-7}$	0.0000320	0	$9.91 \times 10^{-6}$	0
4b	0.288	-0.000578	0.0149	-0.00105	$9.26 \times 10^{-7}$	0.0000313	$-2.11 \times 10^{-6}$	0.0000103	$-1.45 \times 10^{-6}$

Model: O-only

2a levels (meV):  $E_1 = 0.2322, E_2 = 6.977, E_3 = 7.440, E_4 = 9.200, E_5 = 32.44, E_6 = 32.53, E_7 = 33.10$ 4b levels (meV):  $E_1 = 1.156, E_2 = 7.748, E_3 = 7.973, E_4 = 9.796, E_5 = 33.35, E_6 = 33.50, E_7 = 33.94$ 

Position	$B_2^0$	$B_4^0$	$B_4^3$	$B_4^{-3}$	$B_6^0$	$B_6^3$	$B_6^{-3}$	$B_6^6$	$B_6^{-6}$
2a	0.0190	-0.000688	0.0187	0	$1.23 \times 10^{-6}$	0.0000350	0	0.0000150	0
4b	0.00511	-0.000696	0.0190	-0.00126	$1.34 \times 10^{-6}$	0.0000343	$-2.36 \times 10^{-6}$	0.0000154	$-2.03 \times 10^{-6}$

Model: O-only, with radial factor  $\gamma = 1.1$ 2a levels (meV):  $E_1 = 0.7997, E_2 = 9.299, E_3 = 9.832, E_4 = 11.39, E_5 = 42.19, E_6 = 42.70, E_7 = 43.42$ 4b levels (meV):  $E_1 = 1.818, E_2 = 10.22, E_3 = 10.53, E_4 = 12.08, E_5 = 43.31, E_6 = 43.90, E_7 = 44.49$ 

Position	$B_2^0$	$B_4^0$	$B_4^3$	$B_4^{-3}$	$B_6^0$	$B_6^3$	$B_6^{-3}$	$B_6^6$	$B_6^{-6}$
2a	0.0215	-0.000893	0.0243	0	$1.80 \times 10^{-6}$	0.0000512	0	0.0000220	0
4b	0.00579	-0.000904	0.0246	-0.00163	$1.96 \times 10^{-6}$	0.0000502	$-3.46 \times 10^{-6}$	0.0000226	$-2.96 \times 10^{-6}$

Direct fit to neutron data

2a levels (meV):  $E_1 = 0.850, E_2 = 9.70, E_3 = 10.91, E_4 = 12.55, E_5 = 45.11, E_6 = 45.48, E_7 = 46.34$ 4b levels (meV):  $E_1 = 1.850, E_2 = 10.25, E_3 = 12.50, E_4 = 13.32, E_5 = 48.22, E_6 = 49.65, E_7 = 50.39$ 

Position	$B_2^0$	$B_4^0$	$B_4^3$	$B_4^{-3}$	$B_6^0$	$B_6^3$	$B_6^{-3}$	$B_6^6$	$B_6^{-6}$
2a	0.0186	-0.000910	0.02639	0	$1.77 \times 10^{-6}$	0.0000510	0	0.0000242	0
4b	0.00759	-0.001039	-0.002126	-0.02638	$2.402 \times 10^{-6}$	$-4.908 \times 10^{-6}$	-0.0000684	$-2.772 \times 10^{-6}$	$-3.931 \times 10^{-7}$

CEF (crystal electric field) data obtained from the point-charge models and comparison to the experimental data.

reduced frustration<sup>55</sup>. Based on the magnetization measurements, we estimate that the exchange interactions should be smaller than 0.1 meV, but further measurements would be needed to confirm this.

**2D magnetic order.** Two pieces of information can be extracted from the magnetic heat capacity data in Fig. 4b. First, the peak at  $\sim 0.1$  K does not immediately vanish at small magnetic field, resembling an antiferromagnetic ordering transition. Second, there is a lower, broader peak at  $\sim 0.3$  K, evident at small magnetic field, that moves towards higher temperatures as the field increases. This trend of moving to higher temperature with increasing field suggests that the field is assisting rather than competing with the ordering. Therefore, we associate this broader peak with ferromagnetic fluctuations of the system. Based on this analysis, we propose that  $\text{Ba}_3\text{Er}(\text{BO}_3)_3$  realizes two-sublattice exchange physics, in which the honeycomb lattice spins develop ferromagnetic correlations due to the additional spins at the hexagon centers but eventually order in an antiferromagnetic phase.

**3D magnetic order.** Even if the magnetic order is determined within each layer, nontrivial ordering can still happen between the layers. To study the possible 3D magnetic order we now determine the magnetic symmetry that is consistent with the 2D magnetic order. Within each layer, the magnetic order has three-fold rotation symmetry  $C_3$  and the magnetic mirror symmetry  $M'_x = MT$  (product of the ordinary mirror reflection  $M$  given in Table 1 and time reversal  $T$ ). Furthermore, the two layers of  $\text{Er}^{3+}$  in one unit cell can still have different order configurations: the order on the two layers can be either related by  $2_1$  (the ordinary screw in Table 1) or  $2'_1 = 2_1T$ . Physically, these two cases correspond to antiferromagnetic and ferromagnetic (collinear) order between the layers. The corresponding magnetic space groups are  $P6'_3$  cm and  $P6_3c'$ m<sup>56</sup>, respectively. Note that both cases allow an effective Zeeman field on the 2a spin:

$$H_{\text{Zeeman}} = h^z \sum_i S_{i,2a}^z, \quad (2)$$

where  $h^z$  is the effective Zeeman field allowed by the magnetic space group symmetry at the 2a site. The isothermal magnetization measurement (Fig. 3) observes zero magnetization at zero field for temperatures all the way down to 0.3 K (the lowest temperature reached). One scenario consistent with this is that the two layers order antiferromagnetically, corresponding to the magnetic space group  $P6'_3$  cm.

**Exchange interactions.** In this section we discuss the influence of exchange interactions in the context of the experimental data. Based on the structure and symmetry, a minimal exchange model consists of the Ising hamiltonian

$$H_{\text{Ising}} = J_{2a} \sum_{i \in 2a, j \in 4b} S_i^z S_j^z + J_{4b} \sum_{i, j \in 4b} S_i^z S_j^z + H^z \sum_i S_i^z, \quad (3)$$

with antiferromagnetic interactions  $J_{2a} > 0, J_{4b} > 0$ . (We note that a related model with Heisenberg exchange interaction<sup>57</sup> may also be relevant to our compound  $\text{Ba}_3\text{Er}(\text{BO}_3)_3$ ). This model contains several simpler limits. First, for  $J_{2a} = J_{4b}$  it reduces to the triangular lattice Ising model, which is a canonical problem in statistical physics, famous for its frustration and lack of magnetic order. Second, if we include only  $J_{4b} > 0$  exchange, it reduces to a honeycomb lattice Ising model on the 4b sites, which is unfrustrated and shows an antiferromagnetic ordering transition. The phase diagram of the model (3) at zero-field ( $H^z = 0$ ) can be obtained in closed form and contains three phases<sup>58</sup>. At nonzero field  $H^z > 0$ , the phase diagrams of the two limiting cases above both contain an ordered phase and a disordered phase<sup>59,60</sup>.

We now discuss the experimental heat capacity shown in Fig. 4 in context of exchange physics. Ideally, one would like to explain the following key features of the data: At low field there is a singular peak at about 100 mK presumably reflecting long range ordering. This peak decreases in magnitude with weak fields, and becomes noticeably broader above 0.1 T. Above this field, the now broadened low-temperature peak moves upward in temperature with increasing field. In addition, a second distinct broad high temperature (at around 6.5 K in zero field) peak is present at all

fields up to about 2 T, when the peak originating at low temperature merges with it.

The persistent sharpness of the low- $T$  peak in non-zero fields below 0.1 T, shown in Fig. 4b, suggests that it is antiferromagnetic in nature, distinct from the peak in an Ising ferromagnet which broadens immediately upon application of a field. By contrast, in an antiferromagnet, the ordering peak typically weakens and initially moves to lower temperature upon application of a field, due to the competition of antiferromagnetism, which wishes to anti-align the moments and the field, which tries to align them. At somewhat larger fields, the broadened peak typically reverses direction and increases its temperature, as the Zeeman term increases the thermal energy required to release the magnetic entropy. These behaviors are common to many antiferromagnetic models: The low field suppression of ordering temperature happens in the honeycomb lattice Ising model<sup>61</sup>, and the high field enhancement of the heat capacity peak and peak temperature happens in both the honeycomb lattice and the triangular lattice Ising models<sup>62</sup>.

In the experiment, we indeed observe an initial weakening of the ordering peak, but not a shift to lower temperatures. This is perhaps due to the very low temperature of the measured ordering transition. A broadened low-temperature peak moving to higher temperatures for  $H > 0.15$  T is consistent with the expectations just described. As discussed earlier, the high-temperature 6.5 K peak may originate from the crystal field excitations of the 2a sites.

Given the rough consistency of the picture of weak antiferromagnetism, we briefly consider the nature of the possible ordered state. We further introduce an Ising exchange coupling between the two layers, and the total Hamiltonian is

$$H_{\text{total}} = H_{\text{Ising},u} + H_{\text{Ising},d} + J_{u-d} \sum_i S_i^z S_j^z. \quad (4)$$

In general this model results in three-dimensional ordering. In the case of zero field, its phase diagram is a simple extension of the 2D phase diagram<sup>58</sup>. We conclude that for  $J_{4b} > J_{2a}$ ,  $J_{u-d} > 0$ , it supports the following candidate three-dimensional magnetic structure below the zero field transition: Néel order on the honeycomb lattice decorated with extra spins aligned ferromagnetically on the hexagon centers, while the layers order antiferromagnetically with a two-layer periodicity. Further magnetic measurements below the 100 mK ordering transition will be required to test and refine this proposed structure.

## Conclusions

We successfully synthesized high-quality single crystal samples of  $\text{Ba}_3\text{Er}(\text{BO}_3)_3$ , a compound with an erbium-based triangular lattice. Our low-temperature magnetic measurements unveiled significant anisotropy within this system. The magnetic entropy at zero field, as a function of temperature, displayed two distinct plateaus—one at 2 K and another at 10 K, corresponding to  $R \ln 2$  and  $\frac{4}{3} R \ln 2$  respectively. We've linked these observations to the unique environments occupied by the magnetic ions  $\text{Er}^{3+}$  (specifically, their positions at Wyckoff positions 2a and 4b), which possess distinct symmetry properties and crystal field environments. Our calculations align with this interpretation. Additionally, we delved into the exchange interactions occurring within the ground state doublet. Moreover, our research highlights the presence of a zero-field ordering transition, which we contend is of an antiferromagnetic nature. Several characteristics of the heat capacity can be elucidated within this context.

## Methods

**Sample synthesis and single crystal growth.** Polycrystalline  $\text{Ba}_3\text{Er}(\text{BO}_3)_3$  samples were synthesized using the solid-state

reaction technique.  $\text{BaCO}_3$  (99.95% metal basis, Alfa Aesar),  $\text{H}_3^{11}\text{BO}_3$  (>99 atom %, Sigma Aldrich), and  $\text{Er}_2\text{O}_3$  (99.95%, Alfa Aesar) were used as starting precursor materials. The  $^{11}\text{B}$  isotope of boron was used in the synthesis to allow for neutron measurements with these samples, due to its lower neutron absorption cross section compared to  $^{10}\text{B}$ . Using stoichiometric ratios of the starting materials resulted in some leftover  $\text{Er}_2\text{O}_3$  after sintering, so 10% excess of  $\text{H}_3\text{BO}_3$  and  $\text{BaCO}_3$  by weight were added to account for their loss during synthesis. These were mixed thoroughly in a mortar and pestle and then pressed into a pellet. The pellets were sintered at 500 °C for 12 h to remove any water the powders could have absorbed, and then at 1000 °C for 48 h to complete the reaction. As needed, samples were resintered at 1000 °C with intermediate grindings to achieve the pure phase. Once the pure phase was obtained (see Supplementary Note 1, Supplementary Fig. 1), the powders were pressed into cylindrical rods using a hydrostatic press under 700 bar pressure, in preparation for single crystal growths. The cylindrical rods (known as feed and seed) were sintered at 1130 °C under  $\text{O}_2$  atmosphere in a vertical tube furnace to achieve higher density. These rods were then grown into single crystals using a four-mirror optical floating zone furnace. Growth parameters were refined over the course of several growth attempts and eventually high purity centimeter-sized crystals were grown.

**Magnetic and heat capacity measurements.** Magnetic susceptibility and magnetization were measured from 300 K down to 300 mK using a superconducting quantum interference device (SQUID) magnetometer with  $^3\text{He}$  attachment. Further measurements were carried out using a Quantum Design Dynacool Physical Property Measurement System (QD PPMS). Heat capacity data were taken from room temperature down to 60 mK using helium-4 and dilution refrigerator (DR) options attached to the PPMS.

**Inelastic neutron scattering.** Inelastic neutron scattering (INS) experiments were performed on a powder sample of  $\text{Ba}_3\text{Er}(\text{BO}_3)_3$  on the SEQUOIA spectrometer at Oak Ridge National Laboratory<sup>48</sup> to determine the crystal electric field (CEF) ground state of the compound. Measurements were taken at 5 K, 30 K, and 150 K using incident energy 12 meV, 50 meV, and 150 meV at each temperature. The powder was sealed with helium exchange gas to ensure good temperature coupling. A powder sample of the nonmagnetic analog  $\text{Ba}_3\text{Lu}(\text{BO}_3)_3$  was also measured to use for nonmagnetic background subtraction. The neutron data were analyzed using DAVE<sup>63</sup> and the CEF levels were fit using the Python package PyCrystalField<sup>64</sup>.

## Data availability

The data supporting this study are available from the corresponding author upon reasonable request.

Received: 15 June 2023; Accepted: 9 January 2024;

Published online: 19 January 2024

## References

- Anderson, P. Resonating valence bonds: A new kind of insulator? *Mater. Res. Bull.* **8**, 153–160 (1973).
- Balents, L. Spin liquids in frustrated magnets. *Nature* **464**, 199–208 (2010).
- Li, Y. et al. Gapless quantum spin liquid ground state in the two-dimensional spin-1/2 triangular antiferromagnet  $\text{YbMgGaO}_4$ . *Sci. Rep.* **5**, 16419 (2015).
- Li, Y. et al. Rare-earth triangular lattice spin liquid: A single-crystal study of  $\text{YbMgGaO}_4$ . *Phys. Rev. Lett.* **115**, 167203 (2015).

- Li, Y. et al. Muon spin relaxation evidence for the  $u(1)$  quantum spin-liquid ground state in the triangular antiferromagnet  $\text{YbMgGaO}_4$ . *Phys. Rev. Lett.* **117**, 097201 (2016).
- Zhang, X. et al. Hierarchy of exchange interactions in the triangular-lattice spin liquid  $\text{YbMgGaO}_4$ . *Phys. Rev. X* **8**, 031001 (2018).
- Li, Y.  $\text{YbMgGaO}_4$ : A triangular-lattice quantum spin liquid candidate. *Adv. Quantum Technol.* **2**, 1900089 (2019).
- Ma, Z. et al. Spin-glass ground state in a triangular-lattice compound  $\text{YbZnGaO}_4$ . *Phys. Rev. Lett.* **120**, 087201 (2018).
- Li, Y. et al. Crystalline electric-field randomness in the triangular lattice spin-liquid  $\text{YbMgGaO}_4$ . *Phys. Rev. Lett.* **118**, 107202 (2017).
- Zhu, Z., Maksimov, P. A., White, S. R. & Chernyshev, A. L. Disorder-induced mimicry of a spin liquid in  $\text{YbMgGaO}_4$ . *Phys. Rev. Lett.* **119**, 157201 (2017).
- Parker, E. & Balents, L. Finite-temperature behavior of a classical spin-orbit-coupled model for  $\text{YbMgGaO}_4$  with and without bond disorder. *Phys. Rev. B* **97**, 184413 (2018).
- Ranjith, K. M. et al. Anisotropic field-induced ordering in the triangular-lattice quantum spin liquid  $\text{NaYbSe}_2$ . *Phys. Rev. B* **100**, 224417 (2019).
- Bordelon, M., Kenney, E. & Liu, C. Field-tunable quantum disordered ground state in the triangular-lattice antiferromagnet  $\text{NaYbO}_2$ . *Nat. Phys.* **15**, 1058–1064 (2019).
- Ding, L. et al. Gapless spin-liquid state in the structurally disorder-free triangular antiferromagnet  $\text{NaYbO}_2$ . *Phys. Rev. B* **100**, 144432 (2019).
- Baenitz, M. et al.  $\text{NaYbS}_2$ : A planar spin- $\frac{1}{2}$  triangular-lattice magnet and putative spin liquid. *Phys. Rev. B* **98**, 220409 (2018).
- Guo, J. et al. Magnetic-field and composition tuned antiferromagnetic instability in the quantum spin-liquid candidate  $\text{NaYbO}_2$ . *Phys. Rev. Mater.* **4**, 064410 (2020).
- Liu, W. et al. Rare-earth chalcogenides: A large family of triangular lattice spin liquid candidates. *Chin. Phys. Lett.* **35**, 117501 (2018).
- Bordelon, M. M. et al. Spin excitations in the frustrated triangular lattice antiferromagnet  $\text{NaYbO}_2$ . *Phys. Rev. B* **101**, 224427 (2020).
- Xing, J., Sanjeeva, L. D., May, A. F. & Sefat, A. S. Synthesis and anisotropic magnetism in quantum spin liquid candidates  $\text{AYbSe}_2$  ( $A = \text{K}$  and  $\text{Rb}$ ). *APL Mater.* **9**, 111104 (2021).
- Xing, J. et al. Field-induced magnetic transition and spin fluctuations in the quantum spin-liquid candidate  $\text{CsYbSe}_2$ . *Phys. Rev. B* **100**, 220407 (2019).
- Guo, S., Ghasemi, A., Broholm, C. L. & Cava, R. J. Magnetism on ideal triangular lattices in  $\text{NaBaYb}(\text{BO}_3)_2$ . *Phys. Rev. Materials* **3**, 094404 (2019).
- Sanders, M. B., Cevallos, F. A. & Cava, R. J. Magnetism in the  $\text{KBaRE}(\text{BO}_3)_2$  ( $\text{RE} = \text{Sm}, \text{Eu}, \text{Gd}, \text{Tb}, \text{Dy}, \text{Ho}, \text{Er}, \text{Tm}, \text{Yb}, \text{Lu}$ ) series: materials with a triangular rare earth lattice. *Mater. Res. Express* **4**, 036102 (2017).
- Svetlyakova, T. N. et al. Search for compounds of the  $\text{NaBa}(\text{BO}_3)_2$  family ( $r = \text{La}, \text{Nd}, \text{Gd}$ , and  $\text{Yb}$ ) and the new  $\text{NaBaYb}(\text{BO}_3)_2$  orthoborate. *Crystallogr. Rep.* **58**, 54–60 (2013).
- Pan, B. L. et al. Specific heat and thermal conductivity of the triangular-lattice rare-earth material  $\text{KBaYb}(\text{BO}_3)_2$  at ultralow temperature. *Phys. Rev. B* **103**, 104412 (2021).
- Kuznetsov, A. B. et al. Synthesis and growth of rare earth borates  $\text{NaSrR}(\text{BO}_3)_2$  ( $\text{R} = \text{Ho-Lu}, \text{Y}, \text{Sc}$ ). *Inorganic Chem.* **61**, 7497–7505 (2022).
- Bag, R. et al. Realization of quantum dipoles in triangular lattice crystal  $\text{Ba}_3\text{Yb}(\text{BO}_3)_3$ . *Phys. Rev. B* **104**, L220403 (2021).
- Cevallos, F. A., Stolze, K. & Cava, R. J. Structural disorder and elementary magnetic properties of triangular lattice  $\text{ErMgGaO}_4$  single crystals. *Solid State Commun.* **276**, 5–8 (2018).
- Cevallos, F. A., Stolze, K., Kong, T. & Cava, R. Anisotropic magnetic properties of the triangular plane lattice material  $\text{TmMgGaO}_4$ . *Mater. Res. Bull.* **105**, 154–158 (2018).
- Hashimoto, Y., Wakeshima, M. & Hinatsu, Y. Magnetic properties of ternary sodium oxides  $\text{NaLnO}_2$  ( $\text{Ln} = \text{rare earths}$ ). *J. Solid State Chem.* **176**, 266–272 (2003).
- Xing, J. et al. Synthesis, magnetization, and heat capacity of triangular lattice materials  $\text{NaErSe}_2$  and  $\text{KErSe}_2$ . *Phys. Rev. Mater.* **3**, 114413 (2019).
- Deng, B., Ellis, D. E. & Ibers, J. A. New layered rubidium rare-earth selenides: syntheses, structures, physical properties, and electronic structures for  $\text{RbLnSe}_2$ . *Inorganic Chem.* **41**, 5716–5720 (2002).
- Sanjeeva, L. D., Xing, J., Taddei, K. M. & Sefat, A. S. Synthesis, crystal structure and magnetic properties of  $\text{KLnSe}_2$  ( $\text{Ln} = \text{La}, \text{Ce}, \text{Pr}, \text{Nd}$ ) structures: A family of 2D triangular lattice frustrated magnets. *J. Solid State Chem.* **308**, 122917 (2022).
- Havlák, L., Fábry, J., Henriques, M. & Dušek, M. Structure determination of  $\text{KScS}_2$ ,  $\text{RbScS}_2$  and  $\text{KLnS}_2$  ( $\text{Ln} = \text{Nd}, \text{Sm}, \text{Tb}, \text{Dy}, \text{Ho}, \text{Er}, \text{Tm}$  and  $\text{Yb}$ ) and crystal-chemical discussion. *Acta Crystallogr. Sect. C* **71**, 623–630 (2015).
- Dong, B., Doi, Y. & Hinatsu, Y. Structure and magnetic properties of ternary potassium lanthanide oxides  $\text{KLnO}_2$  ( $\text{Ln} = \text{Y}, \text{Nd}, \text{Sm-Lu}$ ). *J. Alloys Compounds* **453**, 282–287 (2008).
- Kononova, N. et al. Synthesis of new isostructural orthoborates  $\text{NaBa}(\text{BO}_3)_2$  with  $\text{R} = \text{Tb}, \text{Dy}, \text{Ho}, \text{Er}, \text{Tm}$  and  $\text{Lu}$ . *Mater. Res.* **19**, 834–838 (2016).
- Guo, S., Kong, T. & Cava, R. J.  $\text{NaBa}(\text{BO}_3)_2$  ( $\text{R} = \text{Dy}, \text{Ho}, \text{Er}$  and  $\text{Tm}$ ): structurally perfect triangular lattice materials with two rare earth layers. *Mater. Res. Express* **6**, 106110 (2019).
- Guo, S. et al. Triangular rare-earth lattice materials  $\text{RbBa}(\text{BO}_3)_2$  ( $\text{R} = \text{Y}, \text{Gd}, \text{Yb}$ ) and comparison to the  $\text{KBa}(\text{BO}_3)_2$  analogs. *Inorganic Chem.* **58**, 3308–3315 (2019).
- Cai, Y. et al.  $\mu\text{SR}$  study of the triangular Ising antiferromagnet  $\text{ErMgGaO}_4$ . *Phys. Rev. B* **101**, 094432 (2020).
- Gao, S. et al. Crystal electric field excitations in the quantum spin liquid candidate  $\text{NaErSe}_2$ . *Phys. Rev. B* **102**, 024424 (2020).
- Scheie, A., Garlea, V. O., Sanjeeva, L. D., Xing, J. & Sefat, A. S. Crystal-field hamiltonian and anisotropy in  $\text{KErSe}_2$  and  $\text{CsErSe}_2$ . *Phys. Rev. B* **101**, 144432 (2020).
- Xing, J. et al. Stripe antiferromagnetic ground state of the ideal triangular lattice compound  $\text{KErSe}_2$ . *Phys. Rev. B* **103**, 144413 (2021).
- Ding, G. et al. Stripe order and spin dynamics in the triangular-lattice antiferromagnet  $\text{KErSe}_2$ : A single-crystal study with a theoretical description. *Phys. Rev. B* **107**, L100411 (2023).
- Ilyukhin, A. *Russ. J. Inorg. Chem.* **38**, 1625–1630 (1993).
- Khamaganova, T., Kuperman, N. & Bazarova, Z. The double borates  $\text{Ba}_3\text{Ln}(\text{BO}_3)_3$ ,  $\text{Ln} = \text{La-Lu}$ . *J. Solid State Chem.* **145**, 33–36 (1999).
- Cox, J. R., Keszler, D. A. & Huang, J. The Layered Borates  $\text{Ba}_3\text{M}(\text{BO}_3)_3$  ( $\text{M} = \text{Dy}, \text{Ho}, \text{Y}, \text{Er}, \text{Tm}, \text{Yb}, \text{Lu}$ , and  $\text{Sc}$ ). *Chem. Mater.* **6**, 2008–2013 (1994).
- Gao, Y., Xu, L., Tian, Z. & Yuan, S. Synthesis and magnetism of  $\text{RE}(\text{BaBO}_3)_3$  ( $\text{RE} = \text{Dy}, \text{Ho}, \text{Er}, \text{Tm}, \text{Yb}$ ) series with rare earth ions on a two dimensional triangle-lattice. *J. Alloys Compounds* **745**, 396–400 (2018).
- Blundell, S. Magnetism in condensed matter. In: *Oxford Master Series in Condensed Matter Physics* (OUP Oxford, 2001).
- Granroth, G. E. et al. SEQUOIA: a newly operating chopper spectrometer at the SNS. *J. Phys. Conf. Ser.* **251**, 012058 (2010).
- Khatua, J. et al. Magnetic properties of the triangular-lattice antiferromagnets  $\text{Ba}_3\text{RB}_3\text{O}_{18}$  ( $\text{R} = \text{Yb}, \text{Er}$ ). *Phys. Rev. B* **106**, 104408 (2022).
- Stevens, K. W. H. Matrix elements and operator equivalents connected with the magnetic properties of rare earth ions. *Proc. Phys. Soc. Sect. A* **65**, 209–215 (1952).
- Hutchings, M. *Point-charge calculations of energy levels of magnetic ions in crystalline electric fields\*\*this work was supported by the U.S. air force, the U.K. department of and industrial research, and the U.S. atomic energy commission.* vol. 16 of Solid State Physics, 227–273 (Academic Press, 1964).
- Bauer, E. & Rotter, M. Magnetism of complex metallic alloys: Crystalline electric field effects. In *Properties and Applications of Complex Intermetallics*, 183–248 (World Scientific, 2010).
- Jain, A. et al. Commentary: The Materials Project: A materials genome approach to accelerating materials innovation. *APL Mater.* **1**, 011002 (2013).
- Data retrieved from the materials project for  $\text{Ba}_3\text{Er}(\text{BO}_3)_3$  (mp-1214885) from database version v2023.11.1. [https://next-gen.materialsproject.org/materials/mp-1214885?material\\_ids=mp-1214885](https://next-gen.materialsproject.org/materials/mp-1214885?material_ids=mp-1214885). Accessed on January, 2024.
- Gordon, E. E. et al. Nonequivalent spin exchanges of the hexagonal spin lattice affecting the low-temperature magnetic properties of  $\text{RInO}_3$  ( $\text{R} = \text{Gd}, \text{Tb}, \text{Dy}$ ): Importance of spin-orbit coupling for spin exchanges between rare-earth cations with nonzero orbital moments. *Inorganic Chem.* **57**, 9260–9265 (2018).
- Litvin, D. Tables of crystallographic properties of magnetic space groups. *Acta Crystallogr. Sect. A* **64**, 419–424 (2008).
- Yin, X. et al. Magnetic properties of the quasi two-dimensional centered honeycomb antiferromagnet  $\text{GdInO}_3$ . *Phys. Rev. B* **104**, 134432 (2021).
- Diep, H. T., Debauche, M. & Giacomini, H. Exact solution of an anisotropic centered honeycomb Ising lattice: Reentrance and partial disorder. *Phys. Rev. B* **43**, 8759–8762 (1991).
- Wu, F. Y., Wu, X. N. & Blöte, H. W. J. Critical frontier of the antiferromagnetic Ising model in a magnetic field: The honeycomb lattice. *Phys. Rev. Lett.* **62**, 2773–2776 (1989).
- Metcalf, B. Phase diagram of a nearest neighbor triangular antiferromagnet in an external field. *Phys. Lett. A* **45**, 1–2 (1973).
- Kim, S.-Y. Honeycomb-lattice antiferromagnetic Ising model in a magnetic field. *Phys. Lett. A* **358**, 245–250 (2006).
- Saito, Y. & Igeta, K. Antiferromagnetic Ising model on a triangular lattice. *J. Phys. Soc. Japan* **53**, 3060–3069 (1984).
- Dimeo, R. et al. DAVE: A comprehensive software suite for the reduction, visualization, and analysis of low energy neutron spectroscopic data. *J. Res. Natl. Inst. Standards Technol.* **114**, 341 (2009).
- Scheie, A. *PyCrystalField*: software for calculation, analysis and fitting of crystal electric field Hamiltonians. *J. Appl. Crystallogr.* **54**, 356–362 (2021).

## Acknowledgements

Research performed at Duke University is supported by National Science Foundation Grant No. DMR-1828348 and by the DOE, Office of Science, Basic Energy Sciences



under Award No. DE-SC0023405. A portion of this research used resources at the Spallation Neutron Source, a DOE Office of Science User Facility operated by the Oak Ridge National Laboratory. R.B. acknowledges the support provided by Fritz London Endowed Post-doctoral Research Fellowship at Duke University. S.H. acknowledges the support provided by William M. Fairbank chair in Physics at Duke University. C.L. acknowledges the fellowship support of the Gordon and Betty Moore Foundation through the Emergent Phenomena in Quantum Systems (EPiQS) program. L.B. was supported by the DOE, Office of Science, Basic Energy Sciences under Award No. DE-FG02-08ER46524, and by the Simons Collaboration on Ultra-Quantum Matter, which is a grant from the Simons Foundation (651440).

### Author contributions

Research conceived by S.H.; M.E., R.B., S.E.D. and S.H. synthesized samples; M.E., R.B. and S.H. performed magnetic and thermodynamic measurements; M.E., S.E.D., A.I.K. and S.H. conducted neutron scattering experiments; C.L. and L.B. provided theoretical interpretations; M.E., R.B., C.L., L.B. and S.H. wrote the manuscript with comments from all authors.

### Competing interests

The authors declare no competing interests.

### Additional information

**Supplementary information** The online version contains supplementary material available at <https://doi.org/10.1038/s42005-024-01532-w>.

**Correspondence** and requests for materials should be addressed to Sara Haravifard.

**Peer review information** *Communications Physics* thanks Qing-Ping Ding and the other, anonymous, reviewer(s) for their contribution to the peer review of this work.

**Reprints and permission information** is available at <http://www.nature.com/reprints>

**Publisher's note** Springer Nature remains neutral with regard to jurisdictional claims in published maps and institutional affiliations.



**Open Access** This article is licensed under a Creative Commons Attribution 4.0 International License, which permits use, sharing, adaptation, distribution and reproduction in any medium or format, as long as you give appropriate credit to the original author(s) and the source, provide a link to the Creative Commons licence, and indicate if changes were made. The images or other third party material in this article are included in the article's Creative Commons licence, unless indicated otherwise in a credit line to the material. If material is not included in the article's Creative Commons licence and your intended use is not permitted by statutory regulation or exceeds the permitted use, you will need to obtain permission directly from the copyright holder. To view a copy of this licence, visit <http://creativecommons.org/licenses/by/4.0/>.

© The Author(s) 2024